ACS OMEGA

http://pubs.acs.org/journal/acsodf

Article

Electromagnetic Performance of NiMgCuZn Ferrite for Hyperthermia Application in Cancer Treatment

Xinliang Ge, Huan Li, Hui Zheng,* Peng Zheng, Liang Zheng,* and Yang Zhang

Cite This: *ACS Omega* 2023, 8, 16647−16655

Read Online

ACCESS | Metrics & More | Article Recommendations

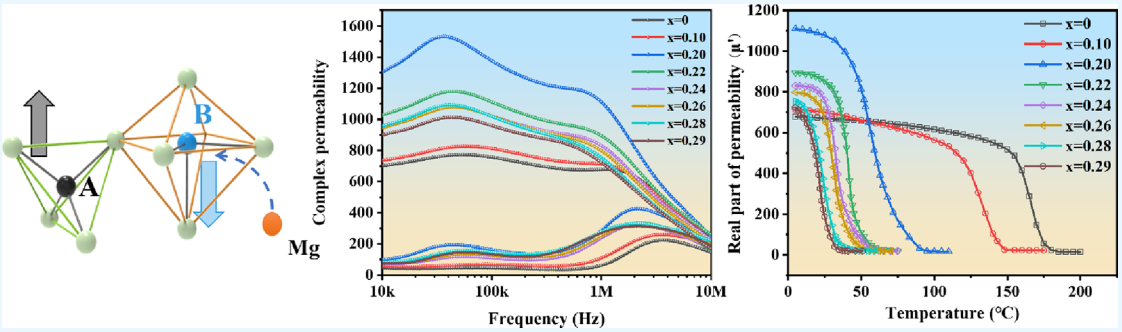

ABSTRACT: Ferrite with high permeability, high magnetic loss, and a low Curie temperature is a highly promising material for hyperthermia applications in cancer treatment. In this work, $Ni_{(0.29-x)}Mg_xCu_{0.14}Zn_{0.60}Fe_{1.94}O_{3.94}$ (NiMgCuZn) ferrites were prepared at different Mg ion concentrations. The dependence of the Mg ion contents on the crystal structure, magnetic, and permeability properties of NiMgCuZn ferrite was investigated. Structural characterization showed a high crystallinity of the materials and an increase in the lattice constant with the Mg ion content. The magnetic hysteresis loops revealed that the saturation magnetization decreased with an increasing Mg content. Furthermore, the permeability measurements showed an increase in permeability and magnetic loss with the doping of Mg. More importantly, the Curie temperature of the NiMgCuZn ferrite decreases with the Mg ion content and reaches 42.37 °C for $x = 0.26$ as well as a real permeability of ∼797.88@1 MHz and a magnetic loss of 0.316@1 MHz, which meet the requirements of tumor hyperthermia.

1. INTRODUCTION

In recent years, the global burden of cancer has been increasing due to aging and population growth. Cancer has become the leading cause of death in developed countries and the second leading cause of death in developing countries.[1−3] The prevention and treatment of cancer has become a major challenge in the field of medicine. Cancer is usually treated with surgical resection, chemotherapy, radiotherapy and biological therapy.[4,5] However, for now, each of these treatments has its own limitations and side effects. These therapies kill cancer cells while causing substantial damage to human cells. On the other hand, it is difficult to completely kill cancer cells, leading to higher recurrence and mortality rates.

Hyperthermia is a method of heating a cancerous part of the body, raising the local temperature to kill the cancer cells. After years of development, hyperthermia has become an important means of cancer treatment.[6,7] Modern medical studies have shown that tumor cells are more sensitive to heat than normal cells.[8] When the temperature of the cancer site in the body is slightly increased to approximately 42 °C, the respiration of tumor cells and the synthesis of DNA, RNA, and protein can be significantly inhibited, thus effectively killing tumor cells.[9] Notably, normal human cells can survive at these temperatures. Compared with other treatment methods, hyperthermia has the characteristics of fewer side effects, less invasiveness, and significant therapeutic effects, which can greatly help improve the quality of life (QOL) of cancer patients.[10]

In the past few years, the application of Fe_2O_3 magnetic nanoparticles in tumor hyperthermia has been investigated.[11,12] Magnetic fluid hyperthermia (MFH) with Fe_2O_3 as the magnetic core can absorb the higher power of the alternating magnetic field but cannot achieve accurate temperature control and easily causes damage to the normal cells of the human body. Therefore, we hope to discover new materials for automatic temperature control to further promote the development of hyperthermia.

Received: November 18, 2022
Accepted: April 26, 2023
Published: May 4, 2023

https://doi.org/10.1021/acsomega.2c07394
ACS Omega 2023, 8, 16647−16655

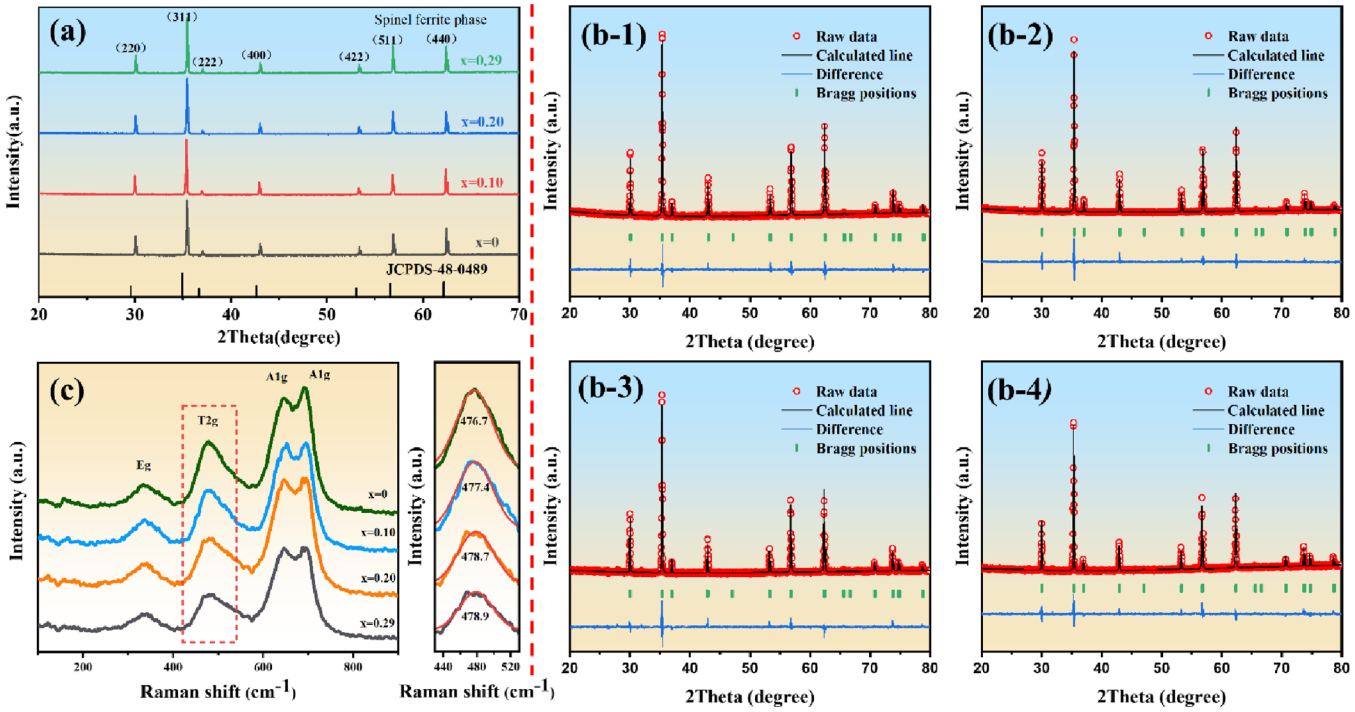

Figure 1. (a) XRD patterns of NiMgCuZn ferrites with different Mg contents (x = 0, x = 0.10, x = 0.20, and x = 0.29); (b) Rietveld refinement of NiMgCuZn ferrites with different Mg contents; (c) Raman spectra of NiMgCuZn ferrite with different Mg contents.

Ferrite materials with low Curie temperature, high permeability, and high-frequency characteristics have attracted extensive attention for their characteristic of automatic temperature control.[13,14] Under the action of the alternating magnetic field, ferrite produces heat due to hysteresis loss. When the temperature of the material exceeds its Curie temperature, it becomes paramagnetic and no more heat is produced. When the heat dissipation of the heating part is below the Curie temperature, the material is transformed into a strong magnetic substance to recover heat production. In this way, the temperature of the treatment site can be controlled around the Curie temperature.

NiCuZn, as a spinel-structured ferrite with high permeability, high resistivity, a low sintering temperature, and a wide application frequency band, has been widely utilized in inductance and microwave devices[15] and shows potential for hyperthermia applications. However, the Curie temperature of NiCuZn ferrite presently exceeds 150 °C, and the low magnetic loss results in low heat generation efficiency, which cannot meet the requirements of hyperthermia.[15] How to reduce the Curie temperature of NiCuZn ferrite and improve its heat production efficiency is important for its application in magnetic heat. It has been reported that MgCuZn ferrite and NiCuZn ferrite have similar magnetic properties and that the replacement of Ni ions by Mg ions can effectively reduce the Curie temperature of NiCuZn ferrite.[16] Moreover, using Mg instead of expensive Ni can greatly reduce the manufacturing cost of NiCuZn ferrite.

In this work, the Curie temperature and permeability of NiCuZn ferrite were improved by the Mg ion doping method. $Ni_{(0.29-x)}Mg_xCu_{0.14}Zn_{0.60}Fe_{1.94}O_{3.94}$ ferrite materials with different Mg ion concentrations were prepared by the solid-phase method. Simultaneously, 0.3 wt % Bi_2O_3 was introduced as an additive to promote grain growth and to improve the electromagnetic properties of ceramics. The dependence of the Mg ion contents on the morphology, crystal structure, magnetic, and permeability properties was analyzed in detail.

2. EXPERIMENTAL SECTION

2.1. Preparation of NiMgCuZn Ferrite. In this experiment, NiMgCuZn ($Ni_{(0.29-x)}Mg_xCu_{0.14}Zn_{0.60}Fe_{1.94}O_{3.94}$) ferrite ceramics were prepared by a low-temperature solid-state reaction, with x = 0, 0.10, 0.20, 0.22, 0.24, 0.26, 0.28, and 0.29. First, the raw materials (NiO (99%), CuO (99%), ZnO (99.8%), MgO (99.9%), and Fe_2O_3 (99.9%) (Aladdin reagent, Shanghai, China)) with accurate quality were weighed according to the chemical formula. Second, these powders were mixed with ethanol (AR grade, 99.9%), put into a planetary ball mill, and stirred at 225 rpm for 12 h. The raw material was dried in an oven, put into an alumina crucible, and preburned at 800 °C for 3 h in air. A previous study has revealed that introducing additives of 0.3 wt % Bi_2O_3 to ferrites can effectively decrease the sintering temperature of NiCuZn ferrites.[17] In the experiment, the preburned powder was weighed, and 0.3 wt % Bi_2O_3 was added according to the weight. After mixing, ethanol as the ball milling medium was put into the planetary ball mill and stirred at 225 rpm for 12 h. After drying again, 5 wt % polyvinyl alcohol (PVA) and 2.5 wt % H_2O (water) were added as binders to granulate the powder. At a pressure of 10 MPa, these particles were pressed into annular samples. Lastly, annular samples and flake samples were sintered at 950 °C for 3 h in air (heating rate: 4 °C/min) by a traditional low-temperature sintering process.

2.2. Characterization Analysis. X-ray diffraction (XRD, Rigaku Co., Tokyo, Japan) was utilized to analyze the crystal structure of the powder samples. The density of each sample was measured by the Archimedes method. Scanning electron microscopy (SEM, JEOL JSM6460) and transmission electron microscopy (TEM, JEOL JEM2100) were employed to obtain the internal microstructure images of the samples, and energy-

https://doi.org/10.1021/acsomega.2c07394
ACS Omega 2023, 8, 16647−16655

dispersive spectroscopy (EDS) was employed to analyze the content and distribution uniformity of each element in the sample. X-ray photoelectron spectroscopy (XPS, Thermo Avantage ESCALAB 250 Xi) was performed to examine the chemical states and elemental composition of various ions in the materials. The crystal structure of NiCuZn was analyzed by Raman scattering spectra of Renishaw confocal Raman spectroscopy with an output power of 514 nm and 10 MW (Renishaw, Gloucestershire, gl127 DW, United Kingdom). The magnetic hysteresis loop of the sample was measured by a vibrating sample magnetometer (VSM, Lake Shore 7410).

The annular sample was wound on the coil and heated by an HP4275A magnetic core oven. The permeability and Curie temperature of the samples were obtained by measuring the inductance of the magnetic ring sample at different temperatures with an impedance analyzer (Agilent E4991B). The permeability of the magnetic ring was calculated by eq 1:

$$\mu = \frac{L \times 10^7}{2N^2 \cdot d \cdot \ln(r_1/r_2)} \quad (1)$$

where L is the inductance value measured by the impedance analyzer, N is the number of turns of the coil ($N = 15$), d is the thickness of the magnetic ring, and r_1 and r_2 are the outer diameter and inner diameter of the magnetic ring, respectively.

3. RESULTS AND DISCUSSION

Figure 1a shows the XRD patterns of NiMgCuZn ferrites doped with 0.3 wt % Bi_2O_3 at different Mg doping concentrations. All the observed diffraction peaks match the NiCuZn ferrite standard PDF card (JCPDS no. 48-0489), and no obvious heterophase exists. To further investigate the effect of the Mg content on the crystal structure of the samples, Rietveld analysis was performed on each sample using FullProf. The refined spectrogram is shown in Figure 1b-1−b-4, and the lattice constant (a), R-factor, and X-ray density are shown in Table 1. XRD data were refined by minimizing differences between observed powder diffraction patterns and modeled powder diffraction patterns. This minimization is carried out with three main reliability index parameters: the contour factor (R_p), weighting factor (R_{wp}), and goodness-of-fit index (χ^2).[17] R_{wp} depends on the difference between the calculated diffraction pattern and the measured diffraction pattern. R_p is the expected minimum value of R_{wp}. χ^2 is the ratio of R_{wp} to R_p. Table 1 shows that the fitting parameters (R_p, R_{wp}, and χ^2) of the samples are small, indicating that the refinement results are within the reliable range and exhibit high quality. The lattice constant increases from 8.410 to 8.429 Å with an increasing Mg doping concentration from $x = 0$ to 0.29. The reason for this increase can be ascribed to the larger ionic radius of the Mg^{2+} ion (0.72 Å) than that of the Ni^{2+} ion (0.69 Å), which results in lattice expansion and an increase in the lattice constant (a) after the substitution of Mg^{2+} for the Ni^{2+} ion.

Table 1. Cation Distribution, Lattice Parameters, and Fitting Parameters (R_p, R_{wp}, and χ^2) of Samples with Different Mg Contents

x	R_p (%)	R_{wp} (%)	χ^2	lattice parameters ($a = b = c$, Å)	d_x (g/cm^3)
0	1.28	2.13	1.08	8.410	5.304
0.10	1.32	2.29	1.06	8.413	5.298
0.20	1.22	2.07	1.02	8.421	5.283
0.29	1.26	2.08	1.16	8.429	5.269

Figure 1c shows the Raman spectra of NiMgCuZn ferrites with different Mg contents to further characterize the structural changes of ions in spinel ferrites. Three first-order Raman activation patterns, namely, A_{1g}, E_g, and T_{2g}, are observed. The A_{1g} mode is caused by the symmetrical stretching of oxygen atoms along Fe−O bonds. The E_g mode is attributed to the symmetrical bending of oxygen with respect to Fe, while the T_{2g} mode is attributed to the asymmetric stretching of Fe.[18] In cubic spinel ferrites, activity patterns above 600 cm^{-1} are generally associated with the movement of oxygen in the tetrahedral group (A site),[19] and patterns below 600 cm^{-1} indicate characteristics of the ferrite octahedral group (B site).[20,21] In this study, the use of Mg ions instead of Ni ions had a minimal effect on the peak positions of the A_{1g} and E_g modes, while a significant rightward shift for the T_{2g} mode reflects the characteristic change in the B site of ferrite. This finding can be ascribed to the Mg ions replacing the Ni ions that previously occupied the B site, thus affecting the structural features of the B site.

The surface morphology of the ceramics is also given in the SEM images in Figure 2a−d, which shows that the NiMgCuZn ferrite ceramics formed as dense sintered bodies with high crystallization, regardless of the Mg content. It is confirmed that the solid-phase reaction has adequately occurred at a sintering temperature of 950 °C, which is mainly controlled by grain boundary migration and diffusion.[22,23] The surface morphology also displays a dual microstructure with the coexistence of large and small grains (displayed on the right of Figure 2a), which is beneficial for realizing a highly dense structure. The obtained high crystallinity and dense ceramic at low sintering temperatures can be ascribed to the addition of Bi_2O_3, which has a low melting point and promotes grain boundary migration and diffusion.[24] Bi_2O_3 is distributed on the surfaces of growing grains and can push the pores toward the grain boundary, making it easier for the pores to escape from the grain boundary and further reducing the porosity.[17]

Additionally, Figure 2e−g shows the fracture surfaces of representative NiMgCuZn ferrite ceramics at $x = 0$, 0.1, and 0.2. This finding further confirms that the obtained NiMgCuZn ferrite ceramics have a sintered compact microstructure that is dominated by large grains that are evenly distributed in the microstructure. This finding is also evidenced by the volumetric densities of NiMgCuZn ferrites with different Mg contents in Table 2. When $x = 0$, the volume density of NiCuZn ferrite is 5.22 g/cm^3 and the relative density exceeds 96%. The volume density of the sample gradually decreases with increasing Mg substitution because of the higher atomic weight of Ni (58.69 amu) than Mg (24.31 amu). The densification degree is also closely related to grain growth and the number of pores.[25,26] As observed on the fracture surface, the porosity in these three samples is similar, which is mainly influenced by the process of eliminating PVA (polyvinyl alcohol) and independent of the Mg ion doping concentration.[16] This finding also explains why the sample volume density in Table 2 is lower than the X-ray density in Table 1. The removal of the pores and a further increase in the densification of the ceramic are significant and long-term work.

Figure 2h,i shows the detailed microstructure of representative NiMgCuZn ferrite ceramics at $x = 0$ and 0.26. The TEM images further show a high crystalline quality of the NiMgCuZn ferrite. The high-resolution TEM images show

https://doi.org/10.1021/acsomega.2c07394
ACS Omega 2023, 8, 16647−16655

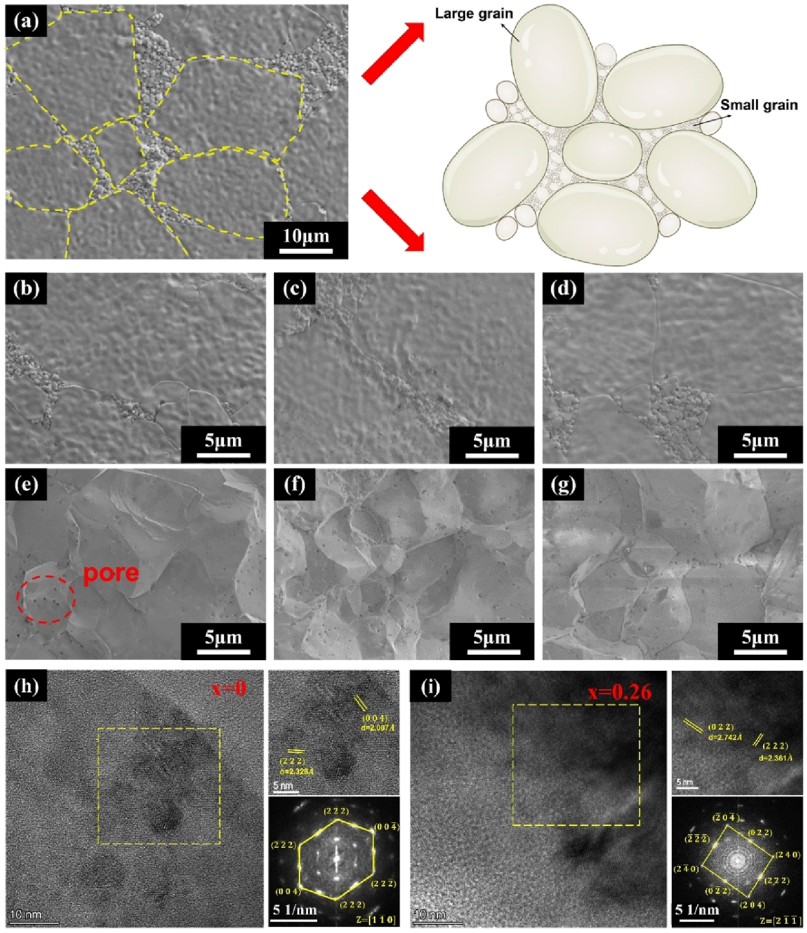

Figure 2. SEM images of the NiMgCuZn ferrite ceramic surface and fracture surface with different Mg contents: (a) x = 0, (b) x = 0.10, (c) x = 0.20, and (d) x = 0.29; (e) fracture surface of x = 0; (f) fracture surface of x = 0.10; (g) fracture surface of x = 0.20. High-resolution TEM images of NiMgCuZn ferrite with different Mg contents and corresponding fast Fourier transform images: (h) x = 0 and (i) x = 0.26.

Table 2. Volumetric Density, Saturation Magnetization, Real Permeability, Curie Temperature, and Magnetic Loss of Samples with Different Mg Contents

x	density (g/cm^3)	M_s (emu/g)	μ' (@1 MHz)	T_c (°C)	tan $\delta\mu$ (@1 MHz)
0	5.218	59.27	678.07	181.52	0.092
0.10	5.184	55.91	712.73	151.57	0.155
0.20	5.104	47.49	1110.66	78.57	0.259
0.22	5.092	44.58	894.21	50.06	0.267
0.24	5.082	41.61	830.48	46.25	0.287
0.26	5.061	39.05	797.88	42.37	0.316
0.28	5.048	37.08	753.53	33.57	0.369
0.29	5.021	35.95	722.54	29.66	0.375

that ferrite ceramics with different Mg contents have well-defined crystal structures, with layer spacings of 2.328 and 2.361 Å for the (222) crystal planes at x = 0 and 0.26, respectively. An increase in the layer spacing was observed after being replaced by Mg ions, which is consistent with the increase in lattice constants in Table 1. The selected electron diffraction patterns of ferrite ceramic and their indexing results are also shown in Figure 2h,i, which displays good crystallinity and a standard cubic spinel structure of the NiMgCuZn ferrite.

Figure 3a–g shows the distribution of elements on the surface of the sample at x = 0.26. All measured elements (including Fe, O, Zn, Ni, Cu, and Mg) are uniformly distributed in the sample, which has an important impact on the electromagnetic performance of the sample. Figure 3h shows that the atomic ratio of the measured elements also corresponds to the theoretical value.

The XPS spectra of the NiMgCuZn ferrite at x = 0.26 were recorded and analyzed to confirm the oxidation states and chemical composition of the elements in the sample. It can be clearly observed from the XPS full spectrum in Figure 3i that Zn, Ni, Fe, and Cu are in the 2p state, that Bi is in the 4f state, and that O and Mg are in the 1s state. The high-resolution Mg 1s, Zn 2p, Cu 2p, Ni 2p, Fe 2p, O 1s, and Bi 4f spectra are shown in Figure 3j–p, respectively. The spectrum of Cu 2p shows the appearance of two peaks. The two peaks at 932.22 and 952.02 eV belong to the $2p_{3/2}$ and $2p_{1/2}$ states. The Cu $2p_{3/2}$ at 932.22 eV decomposed into two peaks: the first peak at 932.05 eV for $Cu^{2+}$and the second peak at 932.63 eV for Cu^{+}. Similarly, the peak at 952.02 eV was decomposed into 951.84 and 952.91 eV corresponding to the peaks of Cu^{2+} and Cu^{+}.[27] The spectra of Fe 2p show peaks at 709.87 and 723.62 eV, which represent the $2p_{3/2}$ state and $2p_{1/2}$ state of Fe ions, respectively. The peak at 709.87 eV decomposed into two peaks: 709.62 eV for Fe^{2+} and 711.46 eV for Fe^{3+}. Similarly, the peak at 723.62 eV decomposed into two peaks at 723.15 and 725.53 eV, corresponding to the peaks of Fe^{2+} cations and Fe^{3+} cations, respectively.[28,29] The high-resolution Ni 2p spectrum shows four peaks at 853.24, 861.19, 872.66, and 877.6 eV. The peak value at 853.24 shows a $2p_{3/2}$ state and confirms the

https://doi.org/10.1021/acsomega.2c07394
ACS Omega 2023, 8, 16647−16655

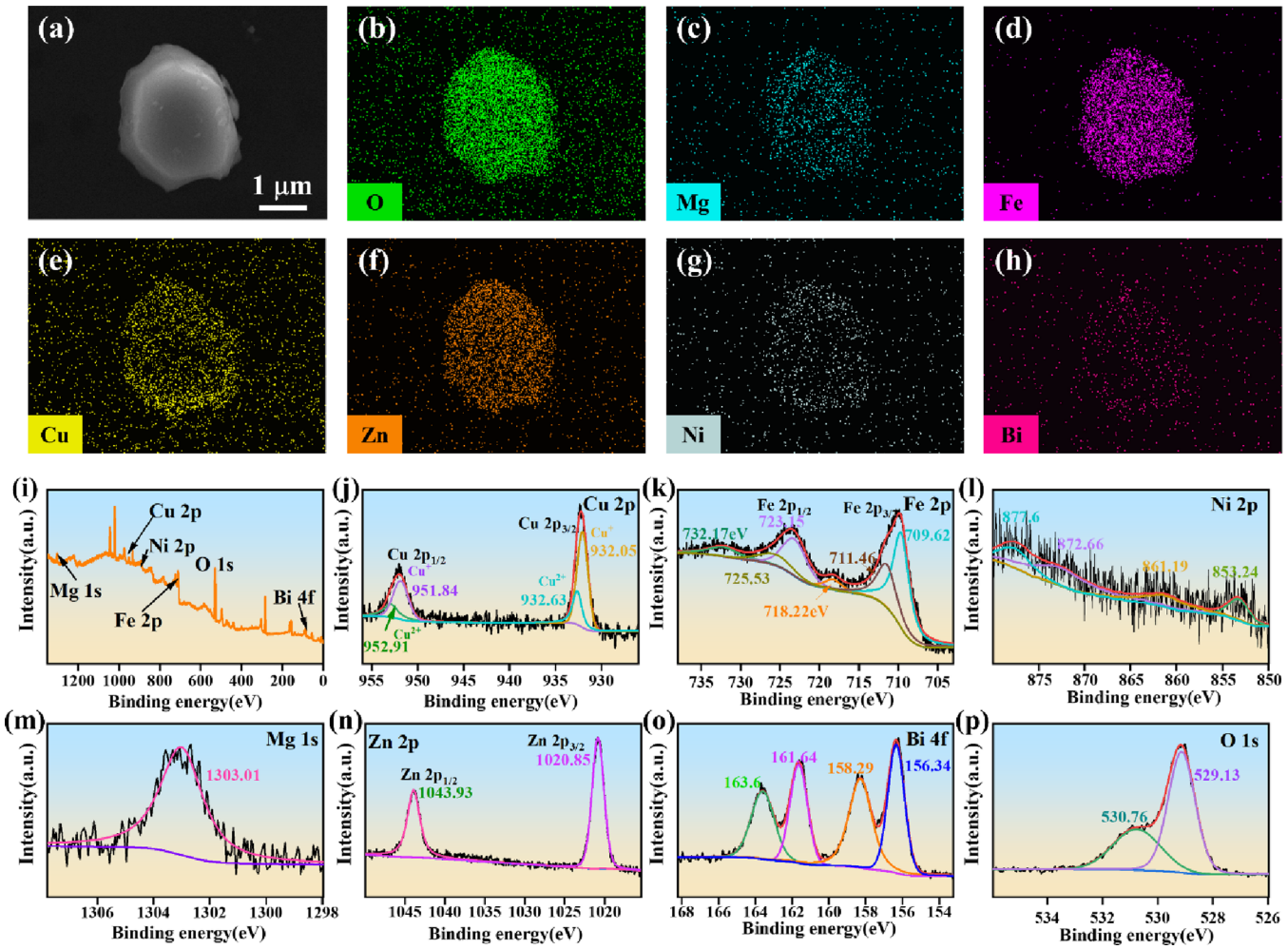

Figure 3. EDS mapping analysis of NiMgCuZn ferrite at $x = 0.26$: (a) SEM image, (b) O, (c) Mg, (d) Fe, (e) Cu, (f) Zn, (g) Ni, and (h) Bi. XPS spectra of different elements in a sample at $x = 0.26$: (i) full-spectrum, (j) high-resolution Cu 2p, (k) high-resolution Fe 2p, (l) high-resolution Ni 2p, (m) high-resolution Mg 1s, (n) high-resolution Zn 2p, (o) high-resolution Bi 4f, and (p) high-resolution O 1s.

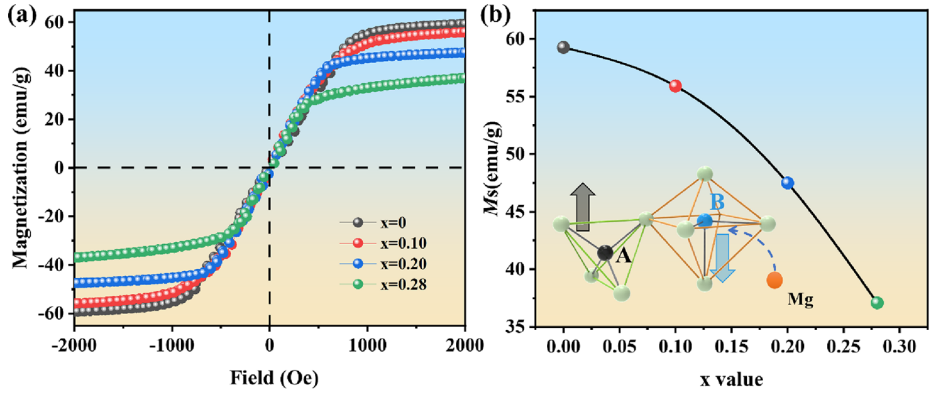

Figure 4. (a) Hysteresis loops of NiMgCuZn ferrites with different Mg contents. (b) Relation of M_s with the x value.

existence of Ni^{2+} ions.[30] A peak is observed in the spectrum of Mg 1s, which is located at 1303.01 eV, confirming the presence of Mg^{2+} ions. Of the two peaks observed in the Zn spectrum, the peak at 1020.85 eV belongs to $2p_{3/2}$, and the peak at 1043.93 eV belongs to the $2p_{1/2}$ state of the Zn^{2+} cation.[31] The Bi spectra showed four peak values of binding energies at 156.34, 158.29, 161.64, and 163.6 eV. The peak values at 158.29 and 163.6 eV correspond to Bi^{3+} ions in the $4f_{7/2}$ state and $4f_{5/2}$ state, respectively. The peaks at 156.34 and 161.64 eV correspond to zero-valent Bi in the $4f_{7/2}$ state and $4f_{5/2}$ state, respectively.[32] The O 1s spectra show two peaks at 529.13 and 530.76 eV, corresponding to $M^{2+}-O^{2-}/M^{3+}-O^{2-}$ bonds (O_L) and oxygen vacancies (O_{ab}), respectively.[33]

The hysteresis loops of NiMgCuZn samples with different Mg contents are measured by a vibrating sample magnetometer; the results are shown in Figure 4a. It is evident that all samples have typical ferrite hysteresis loops and soft ferrite characteristics with a coercivity less than 50 Oe. The saturation

https://doi.org/10.1021/acsomega.2c07394
ACS Omega 2023, 8, 16647−16655

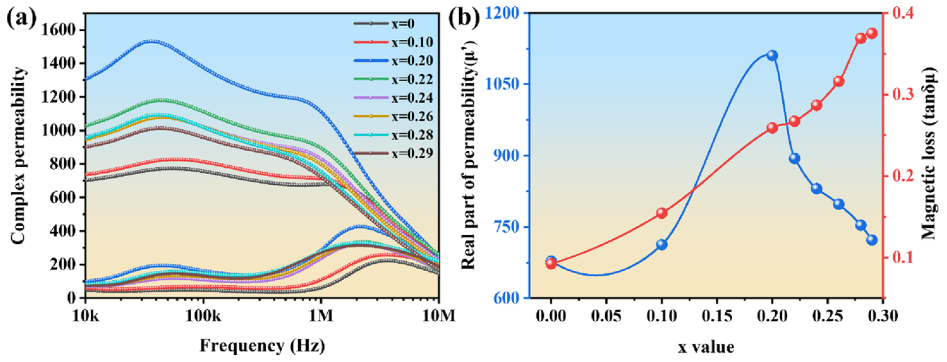

Figure 5. (a) Complex permeability (μ' and μ'') of NiMgCuZn ferrites at different Mg contents; (b) relation of μ' and tan $\delta\mu$ of NiMgCuZn ferrites with different Mg contents at 1 MHz.

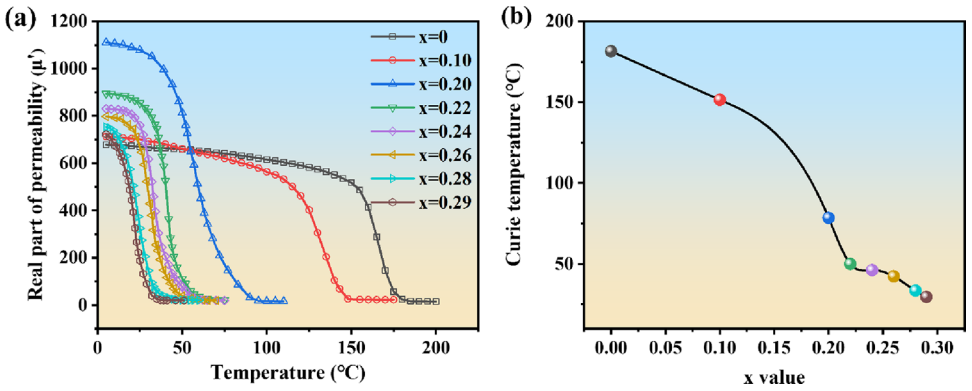

Figure 6. (a) Temperature dependence of the real part of the permeability of NiMgCuZn ferrite with different Mg contents; (b) relation of T_c with x values.

magnetization (M_s) of ferrite is dependent on the Mg content. The changing curve displayed in Figure 4b shows that the saturation magnetization decreases with an increasing Mg content. The reason for this phenomenon is illustrated as follows: The magnetic moment of Ni ions is 2.3 μB, while that of Mg ions is 0 μB.[16] Both Mg ions and Ni ions tend to occupy the octahedral B site. When Mg ions replace Ni ions, the magnetic moment of the B site decreases and the super-exchange between A and B is weakened, leading to a decrease in saturation magnetization. The antiferromagnetic coupling between the A and B positions and the net magnetic moment M is according to $M = M_B - M_A$. When the magnetic moment at position B decreases, there is no change in the magnetic moment at position A, leading to a decrease in the net magnetic moment M and saturation magnetization.

Figure 5a shows the relationship between the real part (μ') and the imaginary part (μ'') of the complex permeability as a function of the frequency for the NiMgCuZn ferrites with different Mg contents. Figure 5b shows the real part of the permeability and the magnetic loss of NiMgCuZn ferrite as a function of x at 1 MHz.

First, μ' increased from 678.07 to 1110.66 at $0 \le x \le 0.20$ and then decreased to 722.54 at $x = 0.29$. Additionally, an increase in permeability leads to a decrease in the cutoff frequency, which is consistent with Snoek's law.[34,35] Complex permeability is derived from two magnetization mechanisms: spin rotation and domain wall motion.[36,37] Permeability is defined as eq 2:[36,38]

$$\mu = 1 + \chi_{spin} + \chi_{dw} \quad (2)$$

where χ_{spin} represents the susceptibility of spin rotation and χ_{dw} represents the susceptibility of domain wall motion. For polycrystalline samples with large particle sizes, the effect of spin rotation on permeability is negligible, so the magnetic domain motion has a major impact on the magnetization process.[15,17] Therefore, eq 2 is simplified to eq 3:

$$\mu \approx 1 + \chi_{dw} = 1 + \frac{3}{16}\cdot M_S^{\,2}\cdot D/\gamma_w \quad (3)$$

where M_s is the saturation magnetization, D is the average grain size, and γ_w is the domain wall energy. It has been reported that the anisotropy constants of magnetic crystals are directly proportional to the domain wall energy.[39−41] Notably, the anisotropy constant of Mg ferrite is smaller than that of Ni ferrite,[16] that is, the domain wall energy of Mg ferrite is smaller than that of Ni ferrite. Therefore, the domain wall energy of NiMgCuZn ferrite decreases with an increasing Mg content. Figure 4b shows that the M_s of NiMgCuZn ferrite also decreases with an increasing Mg content. When Mg ions start to replace Ni ions ($0 \le x \le 0.20$), the decrease in the anisotropy constant of NiMgCuZn ferrite is faster than that of the saturation magnetization. According to eq 3, in this stage, the permeability of NiMgCuZn ferrite continuously increases. The magnetic crystal anisotropy constant depends on atomic coordination. The changes in the A and B site ion will affect the magnetic crystal anisotropy constant. With a further increase in Mg ion substitution ($0.20 \le x \le 0.29$), the decrease in the anisotropy constant of NiMgCuZn ferrite is gradually slower than that of the saturation magnetization, so when $0.20 \le x \le 0.29$, the permeability continuously decreases. Therefore, under the combined action of the change in

https://doi.org/10.1021/acsomega.2c07394
ACS Omega 2023, 8, 16647−16655

anisotropic constants and saturation magnetization, the permeability displays a slight increase at $0 \leq x \leq 0.20$ and then decreases at $0.20 \leq x \leq 0.29$.

Second, the magnetic loss ($\tan \delta\mu = \mu''/\mu'$) of NiMgCuZn ferrites is also dependent on the Mg content and displays a rising trend with an increasing Mg content. Magnetic loss consists of hysteresis loss, eddy current loss, and residual loss.[42,43] At 1 MHz, magnetic loss is mainly determined by eddy current loss and residual loss. In addition, the eddy current loss is inversely proportional to the resistivity, which depends on the crystallinity and grain boundaries of NiMgCuZn ferrite.[44,45] Table 1 shows that with an increasing Mg content, the lattice constant increases, which leads to an increase in crystallinity and a decrease in the grain boundary fraction. Therefore, with an increasing Mg content, the resistivity continuously decreases, and the eddy current loss increases. This trend is the main reason for the increase in magnetic loss after replacing Ni^{2+} with Mg^{2+}. When an external magnetic field is applied, magnetic particles (MPs) absorb heat and transfer it to the tumor due to magnetic loss. MPs located at the cancerous site convert magnetic energy to heat energy, which becomes the heat source of the tumor.[46] Mg ion doping leads to increased magnetic loss, which further improves the effect of thermogenesis and increases the efficiency of killing cancer cells.

Figure 6a shows the temperature dependence of the permeability of NiMgCuZn ferrites with different Mg contents at a constant frequency of 1 MHz. The results show that the permeability approximates a constant value and then sharply decreases to the minimum value. The temperature at which the permeability abruptly drops is referred to as the Curie temperature (T_c). T_c values with different Mg contents are shown in Figure 6b. Notably, it was observed that the T_c value gradually decreased with an increasing Mg content. In ferrites, T_c is affected by the strength of the A−B interaction.[47,48] T_c depends on the number of magnetic ions involved in the exchange interaction N_{A-B}. On the other hand, T_c depends on the exchange integral A_{A-B}. The larger the number of ions involved in the exchange interaction, the stronger the superexchange interaction and the higher the Curie temperature. Since Ni^{2+} is a magnetic ion and Mg^{2+} is a nonmagnetic ion, both tend to occupy the B site. After replacing Ni^{2+} with Mg^{2+}, the number of magnetic ions in the B position decreases, that is, the number of magnetic ions involved in the A−B interaction exchange N_{A-B} decreases, leading to the weakening of the A−B superexchange and a decrease in the Curie temperature. Note that the ionic radius of the Mg^{2+} ion (0.72 Å) is larger than that of the Ni^{2+} ion (0.69 Å). When Mg^{2+} replaces Ni^{2+}, the lattice expands and the lattice constant increases. As the distance between A and B increases, the superexchange between A and B weakens, and the Curie temperature drops. Lowering the Curie temperature of ferrite by Mg doping can make it reach the temperature range suitable for tumor hyperthermia (42−47 °C), which is widely believed to be cytotoxic.[49,50] Increasing the temperature of tumor cells from normal body temperature to 42−47 °C for a certain period will yield a high rate of destruction of tumor cells. The Curie temperature of general ferrite is higher, far beyond the range of the human body. In this study, $Ni_{0.03}Mg_{0.26}Cu_{0.14}Zn_{0.60}Fe_{1.94}O_{3.94}$ has a Curie temperature of 42.37 °C and can meet the requirements of tumor hyperthermia.

4. CONCLUSIONS

In this study, the effects of Mg^{2+} doping on the structure, microstructure, and electromagnetic properties of NiMgCuZn ferrite were investigated. Mg^{2+} doping can reduce the Curie temperature of NiMgCuZn ferrite and increase its permeability and magnetic loss. In particular, $Ni_{0.03}Mg_{0.26}Cu_{0.14}Zn_{0.60}Fe_{1.94}O_{3.9}$ has a Curie temperature of ∼42.37 °C, a real permeability of ∼797.88@1 MHz, and a magnetic loss of 0.316@1 MHz, meeting the requirements of tumor thermotherapy. This material can serve as a new thermally sensitive material in magnetic fluid hyperthermia, which can achieve high accuracy of temperature control and greatly simplify the external equipment of the hyperthermia instrument. The suitable Curie temperature allows it to kill cancer cells while reducing the impact on its own cells, and the high permeability and magnetic loss further improve its thermogenesis ability.

AUTHOR INFORMATION

Corresponding Authors

Hui Zheng − *Laboratory for Nanoelectronics and NanoDevices, Department of Electronics Science and Technology, Hangzhou Dianzi University, Hangzhou, Zhejiang 310018, China*; orcid.org/0000-0002-5128-6606; Email: zhenghui0551@hdu.edu.cn

Liang Zheng − *Laboratory for Nanoelectronics and NanoDevices, Department of Electronics Science and Technology, Hangzhou Dianzi University, Hangzhou, Zhejiang 310018, China*; Email: zhengliang@hdu.edu.cn

Authors

Xinliang Ge − *Laboratory for Nanoelectronics and NanoDevices, Department of Electronics Science and Technology, Hangzhou Dianzi University, Hangzhou, Zhejiang 310018, China*

Huan Li − *Laboratory for Nanoelectronics and NanoDevices, Department of Electronics Science and Technology, Hangzhou Dianzi University, Hangzhou, Zhejiang 310018, China*

Peng Zheng − *Laboratory for Nanoelectronics and NanoDevices, Department of Electronics Science and Technology, Hangzhou Dianzi University, Hangzhou, Zhejiang 310018, China*; orcid.org/0000-0003-4327-2308

Yang Zhang − *Laboratory for Nanoelectronics and NanoDevices, Department of Electronics Science and Technology, Hangzhou Dianzi University, Hangzhou, Zhejiang 310018, China*; orcid.org/0000-0002-2337-0683

Complete contact information is available at: https://pubs.acs.org/10.1021/acsomega.2c07394

Author Contributions

X.G., H.Z., and H.L. conceived and designed the project. P.Z., L.Z., and Y.Z. performed the electromagnetic experiments and analyzed the electromagnetic data. H.L. performed the measurements. X.G. and H.Z. analyzed the experimental data and wrote and edited the manuscript with input from all authors. All authors reviewed and contributed to the manuscript.

Notes

The authors declare no competing financial interest.

https://doi.org/10.1021/acsomega.2c07394
ACS Omega 2023, 8, 16647−16655

■ ACKNOWLEDGMENTS

This work is funded by the National Natural Science Foundation of China (Grant No. 51702075).

■ REFERENCES

(1) Lortet-Tieulent, J.; Georges, D.; Bray, F.; Vaccarella, S. Profiling global cancer incidence and mortality by socioeconomic development. *Int. J. Cancer* **2020**, *147*, 3029−3036.
(2) Sung, H.; Ferlay, J.; Siegel, R. L.; Laversanne, M.; Soerjomataram, I.; Jemal, A.; Bray, F. Global cancer statistics 2020: GLOBOCAN estimates of incidence and mortality worldwide for 36 cancers in 185 countries. *Ca-Cancer J. Clin.* **2021**, *71*, 209−249.
(3) Pinheiro, P. S.; Callahan, K. E.; Jones, P. D.; Morris, C.; Ransdell, J. M.; Kwon, D.; Brown, C. P.; Kobetz, E. N. Liver cancer: A leading cause of cancer death in the United States and the role of the 1945−1965 birth cohort by ethnicity. *JHEP Rep.* **2019**, *1*, 162−169.
(4) Yagawa, Y.; Tanigawa, K.; Kobayashi, Y.; Yamamoto, M. Cancer immunity and therapy using hyperthermia with immunotherapy, radiotherapy, chemotherapy, and surgery. *J. Cancer Metastasis Treat.* **2017**, *3*, 218−230.
(5) Galluzzi, L.; Humeau, J.; Buqué, A.; Zitvogel, L.; Kroemer, G. Immunostimulation with chemotherapy in the era of immune checkpoint inhibitors. *Nat. Rev. Clin. Oncol.* **2020**, *17*, 725−741.
(6) Li, H.; Yan, W.; Suo, X.; Peng, H.; Yang, X.; Li, Z.; Zhang, J.; Liu, D. Nucleus-targeted nano delivery system eradicates cancer stem cells by combined thermotherapy and hypoxia-activated chemotherapy. *Biomaterials* **2019**, *200*, 1−14.
(7) Kandasamy, G.; Sudame, A.; Maity, D.; Soni, S.; Sushmita, K.; Veerapu, N. S.; Bose, S.; Tomy, C. V. Multifunctional magnetic-polymeric nanoparticles based ferrofluids for multi-modal in vitro cancer treatment using thermotherapy and chemotherapy. *J. Mol. Liq.* **2019**, *293*, No. 111549.
(8) Wang, W.; Fan, X.; Qiu, J.; Umair, M. M.; Ju, B.; Zhang, S.; Tang, B. Extracorporeal magnetic thermotherapy materials for self-controlled temperature through phase transition. *Chem. Eng. J.* **2019**, *358*, 1279−1286.
(9) Sharma, S. K.; Shrivastava, N.; Rossi, F.; Tung, L. D.; Thanh, N. T. K. Nanoparticles-based magnetic and photo induced hyperthermia for cancer treatment. *Nano Today* **2019**, *29*, No. 100795.
(10) Miyamoto, R.; Saito, H.; Suzuki, M.; Yoshimura, N.; Mitobe, K. Accuracy improvement of low-invasive temperature measurement for hyperthermia treatment using a ferromagnetic implant with low Curie temperature. *Electron. Commun. Jpn.* **2016**, *99*, 55−62.
(11) Lemine, O. M.; Madkhali, N.; Alshammari, M.; Algessair, S.; Gismelseed, A.; Mir, L. E.; Hjiri, M.; Yousif, A. A.; El-Boubbou, K. Maghemite (γ-Fe_2O_3) and γ-Fe_2O_3-TiO_2 nanoparticles for magnetic hyperthermia applications: Synthesis, characterization and heating efficiency. *Materials* **2021**, *14*, 5691.
(12) Shaw, S. K.; Kailashiya, J.; Gangwar, A.; Alla, S. K.; Gupta, S. K.; Prajapat, C. L.; Meena, S. S.; Dash, D.; Maiti, P.; Prasad, N. K. γ-Fe_2O_3 nanoflowers as efficient magnetic hyperthermia and photothermal agent. *Appl. Surf. Sci.* **2021**, *560*, No. 150025.
(13) Eivazzadeh-Keihan, R.; Asgharnasl, S.; Bani, M. S.; Radinekiyan, F.; Maleki, A.; Mahdavi, M.; Babaniamansour, P.; Bahreinizad, H.; Shalan, A. E.; Lanceros-Méndez, S. Magnetic copper ferrite nanoparticles functionalized by aromatic polyamide chains for hyperthermia applications. *Langmuir* **2021**, *37*, 8847−8854.
(14) Hassanzadeh-Tabrizi, S. A.; Norbakhsh, H.; Pournajaf, R.; Tayebi, M. Synthesis of mesoporous cobalt ferrite/hydroxyapatite core-shell nanocomposite for magnetic hyperthermia and drug release applications. *Ceram. Int.* **2021**, *47*, 18167−18176.
(15) Yang, B.; Wang, Z. The structure and magnetic properties of NiCuZn ferrites sintered via a two-step sintering process. *J. Sol-Gel Sci. Technol.* **2016**, *80*, 840−847.
(16) Reddy, M. P.; Madhuri, W.; Ramana, M. V.; Reddy, N. R.; Kumar, K. V. S.; Murthy, V. R. K.; Kumar, K. S.; Reddy, R. R. Effect of sintering temperature on structural and magnetic properties of NiCuZn and MgCuZn ferrites. *J. Magn. Magn. Mater.* **2010**, *322*, 2819−2823.
(17) Ji, X.; Shen, C.; Zhao, Y.; Zheng, H.; Wu, Q.; Zhang, Q.; Zheng, L.; Zheng, P.; Zhang, Y. Enhanced electromagnetic properties of low-temperature sintered NiCuZn ferrites by doping with Bi_2O_3. *Ceram. Int.* **2022**, *48*, 20315−20323.
(18) Awati, V.; Badave, K.; Bobade, D. Effect of Tb^{3+} substitution on structural, optical and magnetic properties of $NiCuZnFe_2O_4$ prepared by sol−gel route. *Indian J. Phys.* **2022**, *96*, 89−101.
(19) Wang, Z.; Schiferl, D.; Zhao, Y.; O'Neill, H. S. C. High pressure Raman spectroscopy of spinel-type ferrite $ZnFe_2O_4$. *J. Phys. Chem. Solids* **2003**, *64*, 2517−2523.
(20) Chandramohan, P.; Srinivasan, M. P.; Velmurugan, S.; Narasimhan, S. V. Cation distribution and particle size effect on Raman spectrum of $CoFe_2O_4$. *J. Solid State Chem.* **2011**, *184*, 89−96.
(21) Yadav, R. S.; Havlica, J.; Kuřitka, I.; Kozakova, Z.; Masilko, J.; Hajdúchová, M.; Enev, V.; Wasserbauer, J. Effect of Pr^{3+} substitution on structural and magnetic properties of $CoFe_2O_4$ spinel ferrite nanoparticles. *J. Supercond. Novel Magn.* **2015**, *28*, 241−248.
(22) Cheng, Q.; Wang, Y.; Zhang, J.; Conejo, A. N.; Liu, Z. The grain growth and grain boundary migrations during solid-phase sintering of Fe_2O_3: Experiments and simulations. *Chem. Eng. Sci.* **2022**, *262*, No. 118038.
(23) Bernard-Granger, G.; Guizard, C. New relationships between relative density and grain size during solid-state sintering of ceramic powders. *Acta Mater.* **2008**, *56*, 6273−6282.
(24) Luo, Q.; Su, H.; Tang, X.; Xu, Z.; Li, Y.; Jing, Y. Effects of Bi_2O_3 addition on power loss characteristics of low-temperature-fired NiCuZn ferrites. *Ceram. Int.* **2018**, *44*, 16005−16009.
(25) Du, J.; Zhou, T.; Lian, L.; Liu, Y.; Du, Y. Two-step sintering of M-type strontium ferrite with high coercivity. *Ceram. Int.* **2019**, *45*, 6978−6984.
(26) Xu, F.; Shi, X.; Liao, Y.; Li, J.; Hu, J. Investigation of grain growth and magnetic properties of low-sintered LiZnTi ferrite-ceramic. *Ceram. Int.* **2020**, *46*, 14669−14673.
(27) Zhuk, N. A.; Krzhizhanovskaya, M. G.; Koroleva, A. V.; Sekushin, N. A.; Nekipelov, S. V.; Kharton, V. V.; Makeev, B. A.; Lutoev, V. P.; Sennikova, Y. D. Cu, Mg Codoped Bismuth Tantalate Pyrochlores: Crystal Structure, XPS Spectra, Thermal Expansion, and Electrical Properties. *Inorg. Chem.* **2022**, *61*, 4270−4282.
(28) Fantauzzi, M.; Secci, F.; Angotzi, M. S.; Passiu, C.; Cannas, C.; Rossi, A. Nanostructured spinel cobalt ferrites: Fe and Co chemical state, cation distribution and size effects by X-ray photoelectron spectroscopy. *RSC Adv.* **2019**, *9*, 19171−19179.
(29) Mugutkar, A. B.; Gore, S. K.; Patange, S. M.; Mane, R. S.; Raut, S. D.; Shaikh, S. F.; Ubaidullah, M.; Pandit, B.; Jadhav, S. S. Ammonia gas sensing and magnetic permeability of enhanced surface area and high porosity lanthanum substituted Co−Zn nano ferrites. *Ceram. Int.* **2022**, *48*, 15043−15055.
(30) Albuquerque, A. S.; Tolentino, M. V. C.; Ardisson, J. D.; Moura, F. C. C.; de Mendonça, R.; Macedo, W. A. A. Nanostructured ferrites: structural analysis and catalytic activity. *Ceram. Int.* **2012**, *38*, 2225−2231.
(31) Bas, S. Z.; Yuncu, N.; Atacan, K.; Ozmen, M. A comparison study of MFe_2O_4 (M: Ni, Cu, Zn)-reduced graphene oxide nanocomposite for electrochemical detection of bisphenol A. *Electrochim. Acta* **2021**, *386*, No. 138519.
(32) Yu, P.; Su, L.; Guo, W.; Xu, J. Broadband infrared luminescence in Bi-doped silicate glass. *J. Non-Cryst. Solids* **2017**, *464*, 34−38.
(33) Patil, A. D.; Patange, S. M.; Dighe, P. M.; Shaikh, S. F.; Rana, A. u. H. S.; Pandit, B.; Jadhav, S. S. Tuning the structural, optical and magnetic properties of NiCuZn ($Ni_{0.4}Cu_{0.3}Zn_{0.3}Fe_2O_4$) spinel ferrites by Nb_2O_5 additive. *Ceram. Int.* **2022**, *48*, 27039−27050.
(34) Huo, X.; Su, H.; Wang, Y.; Li, Y.; Tang, X. Effects of Zn substitution on high-frequency properties of $Ba_{1.5}Sr_{1.5}Co_2$-$xZn_xFe_{22}O_{41}$ hexaferrites. *Ceram. Int.* **2021**, *47*, 17120−17127.
(35) Vinnik, D. A.; Zhivulin, V. E.; Sherstyuk, D. P.; Starikov, A. Y.; Zezyulina, P. A.; Gudkova, S. A.; Zherebtsov, D. A.; Rozanov, K. N.; Trukhanov, S. V.; Astapovich, K. A.; Turchenko, V. A.; Sombra, A. S.

https://doi.org/10.1021/acsomega.2c07394
ACS Omega 2023, 8, 16647−16655

B.; Zhou, D.; Jotania, R. B.; Singh, C.; Trukhanov, A. V. Electromagnetic properties of zinc−nickel ferrites in the frequency range of 0.05−10 GHz. *Mater. Today Chem.* **2021**, *20*, No. 100460.
(36) Tsutaoka, T.; Ueshima, M.; Tokunaga, T.; Nakamura, T.; Hatakeyama, K. Frequency dispersion and temperature variation of complex permeability of Ni-Zn ferrite composite materials. *J. Appl. Phys.* **1995**, *78*, 3983−3991.
(37) Caltun, O. F.; Spinu, L.; Stancu, A.; Thung, L. D.; Zhou, W. Study of the microstructure and of the permeability spectra of Ni−Zn−Cu ferrites. *J. Magn. Magn. Mater.* **2002**, *242-245*, 160−162.
(38) Sun, K.; Liu, H.; Yang, Y.; Yu, Z.; Chen, C.; Wu, G.; Jiang, X.; Lan, Z.; Li, L. Contribution of magnetization mechanisms in nickel−zinc ferrites with different grain sizes and its temperature relationship. *Mater. Chem. Phys.* **2016**, *175*, 131−137.
(39) Varalaxmi, N.; Ramamanohar Reddy, N.; Venkata Ramana, M.; Rajagopal, E.; Murthy, V. R.; Sivakumar, K. V. Stress sensitivity of inductance in NiMgCuZn ferrites and development of a stress insensitive ferrite composition for microinductors. *J. Mater. Sci.: Mater. Electron.* **2008**, *19*, 399−405.
(40) Xiong, Z.; Cao, L. High magnetic-dielectric tunability in Ni nanocrystals embedded $BaTiO_3$ films. *J. Alloys Compd.* **2019**, *785*, 200−205.
(41) Xiong, Z.; Cao, L. Interparticle spacing dependence of magnetic anisotropy and dipolar interaction of Ni nanocrystals embedded in epitaxial $BaTiO_3$ matrix. *Ceram. Int.* **2018**, *44*, 8155−8160.
(42) Ni, J. L.; Hu, F.; Feng, S. J.; Kan, X. C.; Han, Y. Y.; Liu, X. S. Soft magnetic properties of FeSiAl/carbonyl iron composites with high magnetic permeability and low magnetic loss. *J. Alloys Compd.* **2021**, *887*, No. 161337.
(43) Shimizu, K.; Furuya, A.; Uehara, Y.; Fujisaki, J.; Kawano, H.; Tanaka, T.; Ataka, T.; Oshima, H. Loss Simulation by Finite-Element Magnetic Field Analysis Considering Dielectric Effect and Magnetic Hysteresis in EI-Shaped Mn−Zn Ferrite Core. *IEEE Trans. Magn.* **2018**, *54*, 1−5.
(44) Kumar, S. R.; Priya, G. V.; Aruna, B.; Raju, M. K.; Parajuli, D.; Murali, N.; Verma, R.; Batoo, K. M.; Kumar, R.; Narayana, P. V. L. Influence of Nd^{3+} substituted $Co_{0.5}Ni_{0.5}Fe_2O_4$ ferrite on structural, morphological, dc electrical resistivity and magnetic properties. *Inorg. Chem. Commun.* **2022**, *136*, No. 109132.
(45) Jiang, F.; Lan, J.; Wei, Z.; You, B.; Li, J.; Li, Y.; Shi, D.; Xiong, Z.; Zhang, P.; Chen, J. Cooperation effect of indium and vanadium co-doped into bismuth-iron garnets on magnetic properties. *Mater. Res. Express* **2021**, *8*, No. 016104.
(46) Astefanoaei, I.; Dumitru, I.; Chiriac, H.; Stancu, A. Controlling temperature in magnetic hyperthermia with low Curie temperature particles. *J. Appl. Phys.* **2014**, *115*, 17B531.
(47) Yue, Z.; Zhou, J.; Gui, Z.; Li, L. Magnetic and electrical properties of low-temperature sintered Mn-doped NiCuZn ferrites. *J. Magn. Magn. Mater.* **2003**, *264*, 258−263.
(48) Zhu, H.; Shen, W.; Zhu, H.; Jin, Y.; Zhou, H. Influence of B_2O_3−MoO_3 addition on microstructure and magnetic properties of low-temperature-fired NiCuZn ferrites. *Ceram. Int.* **2014**, *40*, 10985−10989.
(49) Yusefi, M.; Shameli, K.; Yee, O. S.; Teow, S.-Y.; Hedayatnasab, Z.; Jahangirian, H.; Webster, T. J.; Kuča, K. Green synthesis of Fe_3O_4 nanoparticles stabilized by a Garcinia mangostana fruit peel extract for hyperthermia and anticancer activities. *Int. J. Nanomed.* **2021**, *Volume 16*, 2515.
(50) Meneses-Brassea, B. P.; Cyr, C. M.; Martinez, I.; Botez, C. E.; El-Gendy, A. A. Facile synthesis of superparamagnetic Fe_3O_4 nanoparticles at therapeutic temperature range for magnetic hyperthermia therapy. *J. Nanopart. Res.* **2020**, *22*, 1−6.

https://doi.org/10.1021/acsomega.2c07394
ACS Omega 2023, 8, 16647−16655